JOURNAL OF GEOPHYSICAL RESEARCH, VOL. 107, NO. A11, 1347, doi:10.1029/2001JA009233, 2002

Electron and proton excitation of the FUV aurora: Simultaneous IMAGE and NOAA observations

V. Coumans, J.-C. Gérard, and B. Hubert
Laboratoire de Physique Atmosphérique et Planétaire, Université de Liège, Belgium

D. S. Evans
NOAA Space Environment Center, Boulder, Colorado, USA

Received 24 December 2001; revised 22 March 2002; accepted 29 March 2002; published 6 November 2002.

[1] The Far Ultraviolet (FUV) imaging system on board the IMAGE satellite provides a global view of the north auroral region in different spectral channels. The Wideband Imaging Camera (WIC) is sensitive to the N_2 LBH emission and NI emissions produced by both electron and proton precipitations. The SI12 camera images the Lyman-α emission due to incident protons only. We compare WIC and SI12 observations with model predictions based on particle measurements from the TED and the MEPED detectors on board NOAA-TIROS spacecraft. Models of the interaction of auroral particles with the atmosphere are used together with the in situ proton and electron flux and characteristic energy data to calculate the auroral brightness at the magnetic footprint of the NOAA-15 and NOAA-16 orbital tracks. The MEPED experiment measures the precipitating particles with energy higher than 30 keV, so that these comparisons include all auroral energies, in contrast to previous comparisons. A satisfactory agreement in morphology and in magnitude is obtained for most satellite overflights. The observed FUV-WIC signal is well modeled if the different spatial resolution of the two sensors is considered and the in situ measurements properly smoothed. The calculated count rate includes contributions from LBH emission, the NI 149.3 nm line, and the OI 135.6 nm line excited by electrons and protons. The proton contribution in WIC can locally dominate the electrons. The comparisons indicate that protons can significantly contribute to the FUV aurora at specific times and places and cannot be systematically neglected. The results confirm the shift of the proton auroral oval equatorward of the electron oval in the dusk sector. We also show that in some regions, especially in the dusk sector, high-energy protons dominate the proton energy flux and account for a large fraction of the Lyman-α and other FUV emissions. *INDEX TERMS:* 0310 Atmospheric Composition and Structure: Airglow and aurora; 2716 Magnetospheric Physics: Energetic particles, precipitating; 2736 Magnetospheric Physics: Magnetosphere/ionosphere interactions; 2704 Magnetospheric Physics: Auroral phenomena (2407); *KEYWORDS:* FUV aurora, IMAGE satellite, NOAA satellite, high-energy protons, Lyman alpha

Citation: Coumans, V., J.-C. Gérard, B. Hubert, and D. S. Evans, Electron and proton excitation of the FUV aurora: Simultaneous IMAGE and NOAA observations, *J. Geophys. Res.*, *107*(A11), 1347, doi:10.1029/2001JA009233, 2002.

1. Introduction

[2] The IMAGE (Imager for Magnetopause-to-Aurora Global Exploration) satellite, launched in March 2000, is a mission for remote sensing simultaneously of all regions of the Earth's magnetosphere. Its main objective is to determine how the magnetosphere responds globally to the changing conditions in the solar wind [*Burch*, 2000]. On board the IMAGE satellite, the FUV imaging system globally observes the north auroral region in the far ultraviolet [*Mende et al.*, 2000]. The imagers are designed to monitor the electron and proton precipitation and discriminate between the two types of particles. The experiment is composed of three different instruments: the Wideband Imaging Camera (WIC) and two Spectrographic Imagers (SI12 and SI13). One characteristic of the FUV imager is its capability to simultaneously observe in all three spectral regions. SI12 is the first FUV imager able to detect incident proton flux without contribution from electrons. The WIC passband covers a spectral region including emissions excited by both protons and electrons.

[3] *Senior et al.* [1987] used simultaneous data obtained with the Chatanika incoherent scatter radar and the Dynamics Explorer 2 (DE 2) and NOAA 6 satellites to relate the locations of the precipitating particles in the evening-sector auroral oval. Auroral luminosities observed with the Dynamics Explorer 1 (DE 1) imager were compared with

Copyright 2002 by the American Geophysical Union.
0148-0227/02/2001JA009233$09.00

simultaneous Chatanika radar observations [*Robinson et al.*, 1989] to determine an empirical relationship between the luminosities measured at FUV wavelengths and the Hall and Pedersen conductances. *Østgaard et al.* [1999] and *Østgaard et al.* [2000] made a similar analysis from POLAR UVI satellite data. Comparisons were made between the precipitation patterns of the high-energy (PIXIE) and low-energy (UVI) electron populations, correlated with ground-based observations and geosynchronous satellite data. *Liou et al.* [1999] compared auroral images from the Polar UVI and simultaneous particle observations from the Defense Meteorological Satellite Program (DMSP) in the afternoon (1300–1600 MLT) sector along the oval in the northern hemisphere to determine the magnetospheric source region of postnoon auroral bright spots. Similarly when in situ measurements of charged particle flux and energy are available, one can model the responses of the FUV imagers from models of the interaction of auroral particles with atmospheric constituents. *Frey et al.* [2001] used in situ particle data from the FAST satellite along two orbits on 24 and 25 June 2000 to model the WIC imager response. A comparison between the modeled WIC response and the observations showed good agreement. It was also demonstrated that in one case protons contributed significantly to the observed signal. *Gérard et al.* [2001] presented a comparison with SI12 observations for one of the two FAST overflights where the simulated SI12 response underestimated the latitudinally integrated brightness. This discrepancy was possibly attributed to high-energy protons above the 30 keV upper limit of the FAST detector, suggesting that higher energy protons could be important in producing this emission. In the present work, we use in situ particle measurements from NOAA-15 and NOAA-16 satellites to verify this possibility and assess the role of proton excitation of FUV emissions. The NOAA measurements offer the advantage of observing electrons in the energy range 50 eV to 1000 keV and protons from 50 eV to 800 keV, including all relevant auroral energies. We are thus able to analyze separately the contribution of protons and electrons in the WIC signal and to assess the importance of the high-energy protons.

[4] The statistical study by *Hardy et al.* [1989] using the DMSP satellite data set indicated that the highest average proton energies are found in the evening sector of the oval, with average energies close to or exceeding 30 keV. Even though energetic protons are not an overall dominant energy source in the high-latitude region, they can be important at given locations and times, particularly near the equatorward boundary of the auroral oval in the afternoon and premidnight sectors as suggested by *Hubert et al.* [2001]. The NOAA-15 orbit is well suited to study the region around 1800 MLT and the evening sector.

[5] In section 2 we first describe the instrumentation characteristics on board IMAGE and NOAA satellites and the in situ data from which we model the emission rates to be compared with the FUV observations. In a second part we describe the models used to calculate the auroral brightness from the particle flux and average energy. Section 2.4 summarizes the methodology of all the comparisons, including the procedure used to extract FUV information along the NOAA satellite track and the comparison of the modeled emission rate based on NOAA data with the FUV observations. In section 3 we present some of the results obtained for WIC and SI12. Section 4 analyzes the role played by high-energy protons in the energy flux and in FUV signals. We finally discuss possible sources of expected errors and model uncertainties.

2. Instrumentation and Models

[6] For this work we used two of the FUV instruments on board the IMAGE satellite: WIC and SI12. Data from the two different particle detectors on board the NOAA satellites were used as well. We first describe these instruments and second the numerical models that calculate the FUV auroral brightness from particle measurements.

2.1. FUV Experiment

[7] The IMAGE satellite is in a highly elliptical orbit with an initial perigee altitude of 1000 km and an apogee of about 7 Re. The WIC imager has a passband between 140–180 nm with a low sensitivity below 140 nm. It is mostly sensitive to the LBH bands and the 149.3 nm NI line excited by electron impact on N_2 and N with a small contribution of the NI 174.3 nm doublet. The WIC response also includes a small contribution from the OI 135.6 nm line. NI and OI excitations are produced by incident primary electrons and protons and secondary electrons colliding with neutral atoms. The LBH emission can also be produced by protons and secondary electrons those protons produce. The WIC CCD camera outputs the information digitally in the form of AD converted 8-bit bytes (AD units). The Spectrographic Imager is a narrow-band imager of far ultraviolet auroral emissions at 121.8 nm and 135.6 nm. In this study, we only consider the SI12 imager, which measures the brightness of the Doppler shifted Lyman-α auroral emission. Precipitating protons colliding with neutral atmospheric constituents can capture an electron and become fast hydrogens. A fraction of fast atoms is produced in the H(2p) state and radiates the Ly α line. The observed line is shifted owing to the relative motion between the emitting atoms and the detector. SI12 efficiently rejects the geocoronal Ly α emission at 121.56 nm and only images proton precipitation [*Mende et al.*, 2001].

2.2. NOAA/MEPED-TED Instruments

[8] The Space Environment Monitor on board the NOAA-TIROS satellites includes two instruments used for this study. The Total Energy Detector (TED) measures the directional energy flux carried toward the atmosphere by electrons and positive ions in the energy range from 50 eV to 20 keV. The measurements are made at two pitch angles within the atmospheric loss cone. These pitch angles are transformed along the magnetic field to 120 km altitude, and an integration of the directional energy fluxes over pitch angle is made to obtain the downward energy flux carried by electrons and protons. The energy fluxes carried by these particles are calculated along the satellite trajectory every 2 s. The TED instrument also identifies the energy band in which the maximum sensor response occurred during the energy sweep. Modeling of the instrument response shows that this energy band generally contains the maximum in the differential energy flux spectrum. This energy band, together with the downward energy flux, is also telemetered every 2 s for both types of particle. No significant difference

Table 1. Characteristic Energies of the TED and MEPED Detectors

Channel Number	Energy range, eV	Proton Energy, keV	Electron Energy, keV
		TED	
1	50–73		
2	73–106		
3	106–154		
4	154–224		
5	224–325		
6	325–473		
7	473–688		
8	688–1000		
9	1000–1454		
10	1453–2115		
11	2115–3075		
12	3075–4472		
13	4472–6503		
14	6503–9457		
15	9457–13753		
16	13753–20000		
		MEPED	
1		30–80	>30
2		80–240	>100
3		240–800	>300

between the characteristic energies associated with the two pitch angles is usually found [*Fuller-Rowell and Evans*, 1987]. Table 1 lists the energy bins from each detector. The combination of the characteristic particle energy and the total energy flux, assuming a particular energy spectral distribution, may be used to define the initial particle energy distribution above the atmosphere. Additionally, the sensors' responses in four energy channels are telemetered every 16 s for electrons and protons. These data have been used to check the validity of the Maxwellian (electrons) or kappa (protons) distributions assumed for the higher time-resolution, but less spectral information, data provided every 2 s.

[9] The Medium Energy Proton and Electron Detector (MEPED) instrument is a set of solid-state particle detectors sensitive to electrons in three integral energy bands, >30 keV, >100 keV, and >300 keV, and to protons in the three differential energy bands 30–80 keV, 80–250 keV, and 250–800 keV. The measurements are made with a 2-s resolution at one particle pitch angle within the atmospheric loss cone and at a second pitch angle near 90°. The MEPED 2-s average proton and electron counts are telemetered separately for each energy channel. The characteristics of both detectors are summarized in Table 1.

[10] The low-energy observations may be combined with the measurements of the more energetic particles from the solid-state detectors to reconstruct the particle energy spectrum over an energy range extending from 50 eV to more than 100 keV. The energy spectrum is reconstructed providing that (1) the energy flux in the 50 eV–20 keV interval matches the TED measurements and (2) the peak energy flux is reached at an energy corresponding to the characteristic energy identified in the TED measurements. For the electron flux, we use a Maxwellian approximation as recommended by *Strickland et al.* [1993]:

$$f(E) = \frac{Q_0}{2\pi E_0^2}\,\frac{E}{E_0}\exp\left(-\frac{E}{E_0}\right), \qquad (1)$$

where E_0 is the characteristic energy of the electrons and Q_0 the total energy flux (in mW/m^2). Equation (1) represents the form of the differential flux we used. The Maxwellian flux peaks at the energy $E_p = 2E_0 = \langle E \rangle$.

[11] In the case of protons, measurements suggest that a kappa distribution provides a better fit to the observed proton energy spectrum. The shape of the kappa function is represented by equation (2):

$$f(E) = \frac{Q_0}{2\pi E_0^2}\,\frac{(\kappa-1)(\kappa-2)}{\kappa^2}\,\frac{E}{E_0}\,\frac{(\kappa E_0)^{\kappa+1}}{(E+\kappa E_0)^{\kappa+1}}, \qquad (2)$$

where E_0 is the characteristic energy of the protons, Q_0 the total energy flux. This flux is maximal at the energy E_p given by:

$$E_p = 2E_0\frac{\kappa}{\kappa-1} = \langle E \rangle \frac{\kappa-2}{\kappa-1}. \qquad (3)$$

The kappa index was determined by fitting the average proton energy spectra given by *Hardy et al.*'s [1989] Figure 7 for Kp = 3 at four different local times [*Hubert et al.*, 2001]. A value of 3.5 was adopted as it provides a reasonably good fit to the data.

[12] Using these approximations, the combination of the measured energy flux between 50 eV and 20 keV and the TED peak energy allows one to extrapolate the total energy flux up to 30 keV. The total energy flux is then calculated by integrating the energy distributions (1) and (2).

$$\phi(E) = \int_0^\infty f(E)EdE \qquad (4)$$

[13] As shown in equations (1) and (2), the function $f(E)$ can be estimated from the total flux between 50 eV and 20 keV and the TED characteristic energy. The total energy flux was calculated with equation (4), assuming that the peak energy in the range 50 eV–30 keV is similar to the one in the range 50 eV–20 keV. The high-energy component of the energy flux is obtained by multiplying the particle flux measured by the MEPED by the mean energy of each channel and summing up the contributions.

[14] For the reconstruction of the electron energy spectrum the Maxwellian flux is truncated at 30 keV and the high-energy tail is replaced by the flux measurements from MEPED. In the case of protons, a kappa distribution is used over the full energy spectrum. The difference between the kappa flux and the MEPED measurements in high-energy channels is added to the kappa flux. In so doing, we obtain a full energy spectrum of precipitating particles every 2 s. Figure 1 presents the proton energy spectrum for 12 August 2000 at 1013:10 UT (case c in Table 2). We compare the kappa distribution we used with a Maxwellian one with the same peak energy. Figure 1 also shows the values measured in channels 4, 8, 11 and 14, which are telemetered every 16 s. We note that the high-energy tail is better reproduced by the kappa flux than by the Maxwellian one. The measured flux for low-energy protons is strongly underestimated by the kappa function. However, the relative importance of channel 4 whose energy band

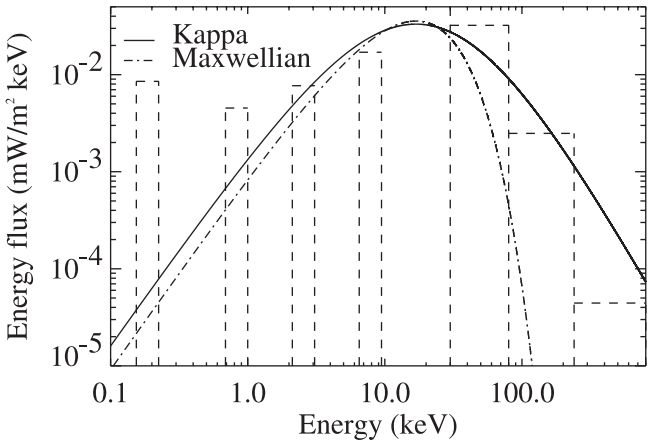

Figure 1. The proton energy flux distribution over the energy range 0.1–800 keV for 12 August 2000 at 1013:10 UT. The solid line shows the kappa ($\kappa = 3.5$) function used in the emission model. The dashed line shows a Maxwellian function with same peak energy and integral flux as the NOAA measurements. Also shown are the energy flux measured in the 3 high-energy channels and in TED low-energy channels 4, 8, 11 and 14.

width is only 70 eV is quite small in comparison with, for example, channel 14 whose width is 2954 eV. The energy flux in the channel 4 is only about 5×10^{-4} mW/m^2 while it is approximately 0.05 mW/m^2 in channel 14. However, the H(2p) excitation cross section is significantly larger at low than higher energy.

2.3. Calculation of Emission and Count Rates

[15] NOAA data are used to reconstruct the electron and proton energy distribution incident at the top of the atmosphere. This distribution serves as an input to auroral emission models to calculate the emission rate profiles. These theoretical profiles are integrated along a line of sight consistent with the viewing geometry of the observations. The instrument response is then used to compute the theoretical count rates which can be compared with the FUV count rates extracted from the observations.

[16] The calculation of the volume excitation rates of the FUV emissions for comparison with the FUV observations is based on two transport models describing respectively the interaction of an electron and a proton beam with the atmosphere. The calculation of auroral electron energy degradation and excitation by electron-induced processes is based on the GLOW model [*Solomon et al.*, 1988] extended to higher energies for auroral calculations [*Hubert et al.*, 2001]. The initial electron energy distribution is assumed to be Maxwellian below 30 keV with a possible high-energy tail derived from the MEPED measurements as described in section 2.2. The error resulting from the use of a single Maxwellian distribution over the full range of electron energies was discussed by *Hubert et al.* [2001]. An estimation of the error based on the electron spectral shape measured with the DMSP detector shows that when using a Maxwellian approximation for electron distribution instead of the sum of two Maxwellian distributions the error varies with the emission wavelength. For example, the calculated LBH emission is 6% higher using the single Maxwellian and can reach up to 30% for OI 135.6 nm emission.

[17] The proton energy transport code was described in detail by *Gérard et al.* [2000]. It is based on the direct Monte Carlo method [*Marov et al.*, 1997] which is a stochastic implementation of the solution of the Boltzmann equations for the H^+ - H beam. Charge exchange collisions of protons with ambient constituents generate a population of fast H atoms which, in turn, may be converted back to energetic protons. The Monte Carlo proton aurora code includes a detailed calculation of all elastic and inelastic processes for both species. A detailed treatment of the momentum transfer in all collisions makes it possible to follow the pitch angle distribution of the simulated particles. Ionization of the major constituents by collisions with energetic H^+ and H particles generates secondary electrons which are treated similarly to the electron-generated secondary population. Many of the proton excitation cross sections for FUV emission are still poorly known or undetermined. Although its volume emission rate is isotropic, the Ly α line profile depends on the relative angle between the magnetic field line and the direction of observation. This effect is accounted for in calculation of the SI12 expected count rate [*Gérard et al.*, 2001].

[18] The temperature profile and the O, O_2 and N_2 densities are calculated from the MSIS-90 model atmosphere [*Hedin*, 1991]. The MSIS input parameters are adapted to the geophysical and geographic conditions of each observation. The ionospheric electron temperature and density used in the calculation of the electron cooling term are taken from the International Reference Atmosphere-1990 (IRI-90) model [*Bilitza*, 1990].

Table 2. Characteristics of the NOAA-TIROS Auroral Oral Crossings

Case	Date	Satellite	Kp	First Peak			Second Peak		
Number	Year 2000			UT	GEOLAT, deg.	MLT, hr-min	UT	GEOLAT, deg.	MLT, hr-min
a	15 Jul.	NOAA-15	6	1227:52	72.80	1805	1241:42	57.09	0835
b	15 Jul.	NOAA-15	6	1409:12	73.29	1836	1423:24	55.41	0802
c	12 Aug.	NOAA-15	7	1014:36	66.68	1746	1030:06	58.65	0910
d	12 Aug.	NOAA-15	7	1158:50	75.66	1739	1211:42	57.02	0843
e	19 Sep.	NOAA-15	5	0921:44	77.07	1627	0927:52	76.68	1155
f	30 Sep.	NOAA-15	3	0142:42	59.63	1753	0154:04	77.39	0926
g	3 Oct.	NOAA-15	4	0033:54	58.45	1817	0046:54	73.92	0842
h	7 Dec.	NOAA-16	3	0519:46	75.23	1144	0531:50	60.65	0343
i	7 Dec.	NOAA-16	2	1854:30	68.47	1151	1906:06	68.81	0253
j	23 Dec.	NOAA-16	4	0558:57	79.73	1117	0609:33	59.48	0329
k	23 Dec.	NOAA-16	4	0740:15	78.05	1220	0753:43	52.54	0242
l	25 Dec.	NOAA-16	3	1405:51	72.64	1347	1416:31	68.39	0156

[19] The volume excitation rates for Ly α, N_2 LBH-bands, OI-135.6 nm and NI in the FUV passbands are integrated with the appropriate view angle to simulate observations by the two FUV imagers. We ignore multiple scattering for the N_2 LBH bands but each line is individually attenuated by O_2 for the appropriate view angle to provide the emergent emission rate. These emerging intensities are folded with the absolute spectral response of the cameras to calculate the expected count rate associated with each auroral pixel. For this purpose, the view angle of the pixel is determined from the orientation of the optical axes of the imagers. The corresponding Ly α line profile is integrated over the SI12 complex transmission function [*Gérard et al.*, 2001].

[20] We use the Monte Carlo model to calculate the efficiency of the high-energy proton channels in SI12 signal. We only consider channels in the energy ranges 30–80 keV and 80–240 keV since higher energy protons make negligible contribution to SI12 for two reasons. First, they produce most of the Ly α photon at very low altitude where the auroral emission is totally absorbed by O_2. Second, the efficiency of the Ly α production drops significantly at high proton energy. The calculation was made with a fixed mean energy in each channel taken as the central value for different view angles. For example, for a vertical observation, the efficiency expressed in count pix^{-1} s^{-1} per incident mW/m^2 in the energy ranges 30–80 keV is 1.75 and in the energy ranges 80–240 keV, the calculated efficiency is 1.06. The efficiency calculation was also made with a random energy in each channel. We used the efficiencies calculated by the second method for this study. For a vertical observation, the calculated efficiency in the energy ranges 30–80 keV with a random energy is 1.5 count pix^{-1} s^{-1} per incident mW/m^2.

2.4. FUV-In Situ Comparisons

[21] The instrumental count rate was extracted for the FUV pixel corresponding to the footprint at 120 km of the magnetic field line at the instantaneous NOAA spacecraft position. An FUV image is obtained every 2 min. During this period, the NOAA spacecraft moves about 850 km along its orbit. To account for this, the count rate from each individual FUV image was extracted along the footprint track of NOAA from the position one minute before to one minute after the central snapshot time. Before extraction of FUV pixels, data were filtered by smoothing by the point spread function (PSF) of the imagers. The width of the PSF was evaluated from the observation of hot stars crossing the field of view: about 3.5 WIC pixels and 2 SI12 pixels. The appropriate FUV pixel from the snapshot was chosen to minimize the difference of the geographic coordinates of the magnetic field line mapped from the NOAA satellite to 120 km and the position of the FUV pixel.

[22] The spatial resolution of the in situ data is much higher than the FUV instrumental resolution. To account for this difference it is necessary to smooth the NOAA data before comparing the modeled intensity with the FUV observation. The NOAA measurements were averaged over a time period corresponding to the combination of the PSF of the FUV instruments with the displacement of the IMAGE satellite along its orbit during the observation. A 1.5 FMHW (6 WIC pixels, 3 SI12 pixels) smoothing width was chosen in consideration of a 66% decrease of the peak of a Gaussian PSF. In a second step, we empirically estimated the smoothing function from comparisons between NOAA and WIC data from one case where the electron incident flux measured by NOAA was very narrow and intense. This comparison provided an upper limit of 120 s of NOAA observation for the smoothing resolution. The NOAA satellites fly over 6 WIC pixels (i.e., 1.5 FMHW) in about 66 s. We thus estimate that the appropriate time period for smoothing the NOAA data is between 66 and 120 s for comparisons with the WIC data. The difference between the theoretical and effective value may stem from the fact that NOAA measurements are made along the orbital track, while FUV globally observes the auroral region. Each FUV pixel includes contributions from emissions adjacent to the NOAA track due to its PSF.

[23] A set of 12 NOAA north polar crossings was selected including 7 NOAA-15 and 5 NOAA-16 orbits. Table 2 lists the dates, UT, MLT and geomagnetic latitudes of the observed first and second peak of electron precipitation. Figure 2 shows the WIC images with the track of the NOAA-15 or NOAA-16 satellites mapped at 120 km. The direction of the spacecraft motion is indicated by an arrow on each image.

3. NOAA-FUV Comparisons

[24] We now present the results of the comparisons, separately for WIC and for SI12.

3.1. WIC Data

[25] Figures 3 and 4 show examples of comparisons between the observed WIC signal and the WIC signal expected from simulation using NOAA in situ measurements. The global form of the observed signal is well reproduced by the model calculation, both in morphology and in intensity. The comparisons have been made after removal of the dayglow background emission by fitting a third degree polynomial to the WIC signal along the NOAA track. The fit is made using WIC data from the region outside the auroral oval, that is inside the polar caps and outside the equatorward boundary of the auroral oval.

[26] Figure 3 shows the observed and the modeled WIC signals illustrated by Figure 2f and whose characteristics are summarized in Table 2-case f. The first oval crossing occurred around 1800 MLT (between 0140 and 0145 UT) and the second oval crossing around 0900 MLT (between 0153 and 0200 UT). The polar cap between 0145 and 0153 UT is characterized by the absence of precipitating particles. The WIC signal corresponding to the oval around 0900 MLT was affected by an important contribution from the dayglow. The difficulty in removing this contribution can explain the somewhat poor agreement with simulated signal in the dayside auroral region and the importance of the error bar. The evaluation of the error on each observation was made in considering the statistical error on the count rates, taking the smoothing of the FUV observation before the pixel extraction into account, and the error induced by the background removal. In Figures 3 and 4 two representative error bars are illustrated. Figure 4 present the comparison illustrated by Figure 2c. In Figure 4, the NOAA spacecraft does not seem to cross any region corresponding to the

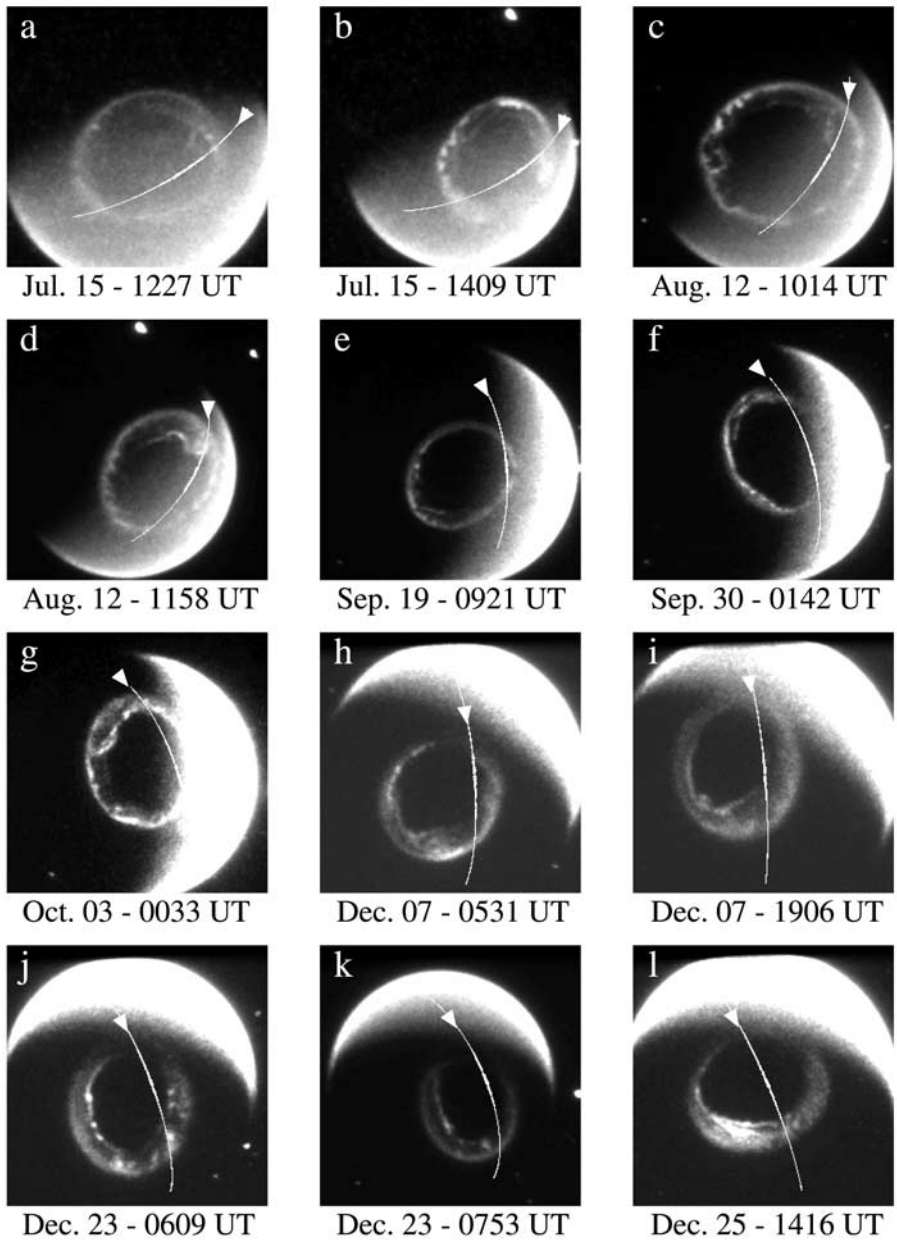

Figure 2. Images taken by the WIC imager. The footprint of the NOAA-TIROS track at 120 km is plotted on each image. For each track the WIC snapshot time was selected to be closest to the time of the electron precipitating energy flux main peak. The arrows show the direction of the NOAA spacecraft motion.

polar cap because of the great extend of the auroral oval and the orbit of the NOAA satellite footprint reached only 78° magnetic latitude and barely entered the polar cap. This example from 12 August 2000 was characterized by a very intense magnetic activity (Kp = 7), which explains the great width of the auroral oval. After 1555 MLT, the observed signal shows oscillations not present in the calculated signal. These variations may also be attributed to the insufficient removal of the background dayglows contribution to the WIC signal in the dayside auroral region. Moreover, Figure 4 shows that the modeled signal around 1800 MLT underestimates the observed WIC signal. The disagreement can locally reach a factor 2. In some other cases (not shown) the simulated WIC signal locally overestimates the observation.

[27] We now statistically compare predicted and observed WIC signal. To avoid uncertainties due to possible inadequate smoothing, we integrate the observed and predicted count rates over the width of the auroral oval crossings. Figure 5 shows the individual data points. All the polar crossing illustrated in Figure 2 were used for this analysis, except case b which was removed from the analysis because

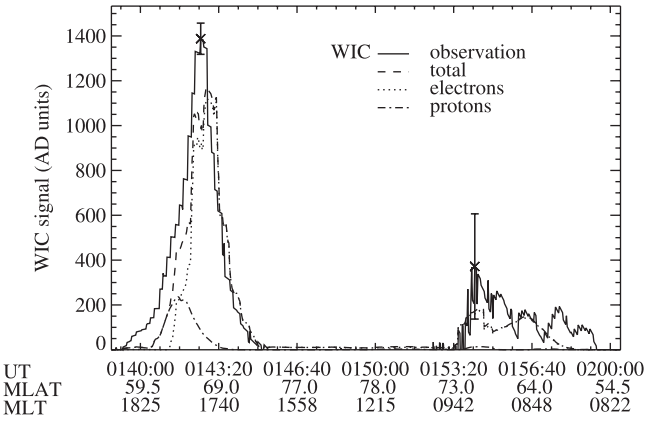

Figure 3. Comparison between the WIC observations (solid line) and a simulated WIC signal based on NOAA particle measurements (dashed line) for case f – 30 September 2000. The modeled contribution of electrons (dotted line) and protons (dotted-dashed line) to the simulated signal are also shown. The error bars represent ± one standard deviation on typical observations.

it was apparently aberrant. The observed count rate was three times larger than the calculated one. A linear least squares fit to these data gives a slope of 0.71 ± 0.06, implying that the calculation slightly underestimates the observation. We estimated the horizontal error bars on each point, that is, the error on the observation. They are found to be comparable to the width of the plot symbols. The dashed line represents the bisecting line corresponding to perfect agreement between simulated and observed signals. Most of the points characterized by a moderate count rate are in quite good agreement with the model. The small discrepancy is principally caused by crossings with large count rates. Possible causes of this difference are discussed in section 4. When removing the NOAA-15 data point of 2.25 $\times$ 10^5 AD units corresponding to case d in Figure 2, the slope becomes 0.89 ± 0.08 (thin solid line in Figure 5), that is quite close to the perfect match.

[28] We now test to what extent thermospheric composition can influence the results of this study. The semiempirical MSIS-90 model [*Hedin*, 1991] is used in the transport models to calculate the temperature and neutral density profiles. This model reproduces the mean thermospheric behavior and does not represent local auroral variations in details. Auroral precipitation produces local heating of the atmosphere causing enhancement of molecular-rich gas in the upper thermosphere. The result of this upwelling is an increase in the N_2/O ratio as confirmed by a large number of observations in the auroral region [*Hecht et al.*, 2000]. As a sensitivity test, we modeled the WIC response assuming the N_2 density was a factor of 2 greater that the MSIS model, in the same time of a doubling of the O_2 density, and compared these results with the outputs using the MSIS model. Figure 6 shows that change corresponding to case i in Table 2. Doubling of the N_2 and O_2 density resulted in an increase in the calculated WIC signal, owing to an increase in the N_2 LBH emission. The increase of O_2 enhances the absorption of the emission and moderate the increase in the calculated signal. In a second test, we reduced the atomic oxygen density by a factor of 2. This decrease in O density had little consequence on the WIC signal. The final case illustrated in Figure 6 shows the results obtained when combining the two perturbations. The result is very close to the doubling N_2 and O_2 result.

[29] This study also provides an opportunity to quantify the role of precipitating protons on N_2 LBH emission. Secondary electrons generated from colliding incident protons contribute to the excitation of N_2 and therefore to the WIC signal. The FUV-in situ comparisons indicate that WIC observations can be dominated by proton contribution. In Figure 4, corresponding to the case c in Table 2, around 1013 UT the contribution of protons locally dominates the contribution of electrons. This feature was also pointed out by *Frey et al.* [2001]. The orientation of the NOAA-15 orbit is well adapted to study the characteristics of the particle precipitation in the dusk sector. As expected from statistical precipitation patterns, the proton oval is generally displaced equatorward of the electron oval in this sector. The proton contribution often explains, in part, the width of the observed WIC oval in the region around 1800 MLT. Model calculations that consider only the electron contribution usually underestimate the WIC signal. A study of the proton contribution to the WIC signal was made by calculating the ratio of simulated WIC counts due to protons to the total WIC counts for the 12 NOAA orbits. The ratios were calculated using 20 seconds s-averaged simulated WIC observations, and neglecting the in situ measurements whenever the total incident energy flux was lower then 0.05 mW/m^2. The study shows the importance of protons in the dusk sector in the equatorward region of the oval: below 65°N, 57% of ratios exceed 0.8 and 82% of the ratios are over 0.1. Above 65°N, only 1% of cases have ratios greater than 0.8 but more than 55% of cases reach 10% of the total contribution. Neglecting the proton contribution in the dusk sector to latitudes under 65°N would introduce errors of over 80% in most cases. In other sectors, the proton contribution would not be so important but it can reach more than 10% in 50% of the cases. We thus conclude that protons cannot be systematically neglected if the WIC signal is to be reliably interpreted in terms of precipitated particle energy flux.

3.2. SI12 Data

[30] Figures 7 and 8 show comparisons between the simulated SI12 signal based on the NOAA data and the

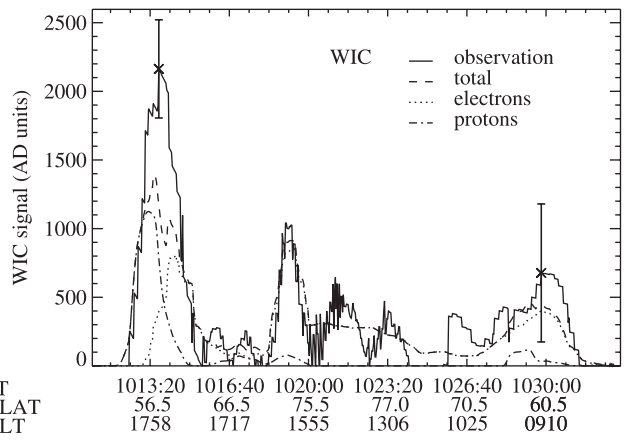

Figure 4. Same as Figure 3 for case c – 12 August 2000.

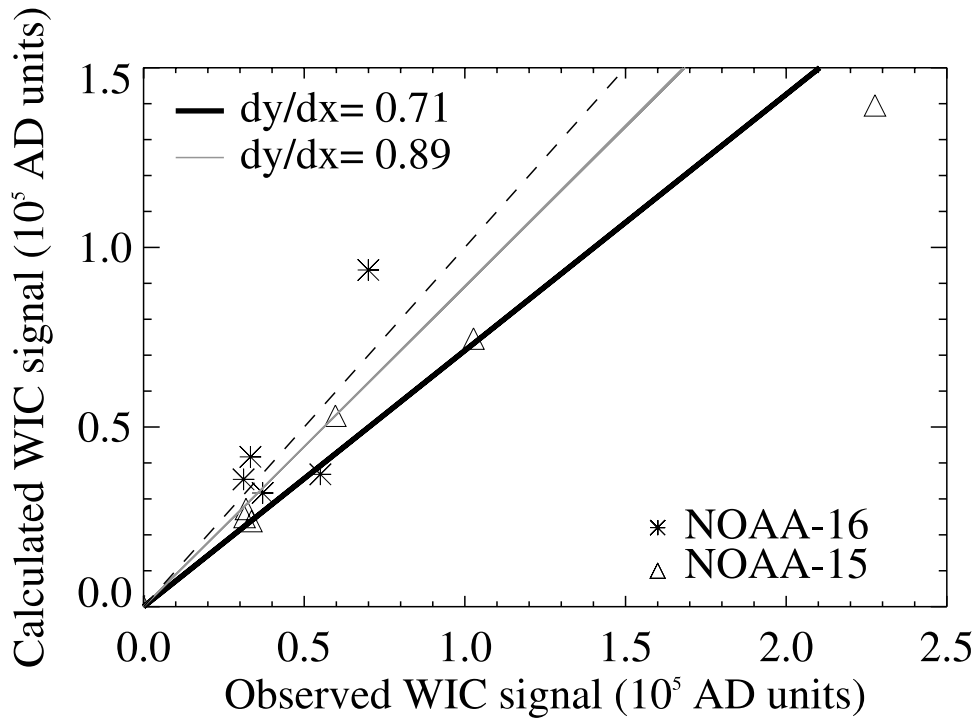

Figure 5. Observed and simulated WIC AD units summed over oval crossing. A least squares regression (bold solid line) gives a slope of 0.71 ± 0.05. The thin solid line shows the least squares regression line when removing the data point at 2.25×10^5 AD units. The slope is then 0.89 ± 0.08. The dashed line corresponds to a perfect agreement between observations and simulations. The size of the horizontal error bars is comparable to the size of the symbol.

actual SI12 observations. In general, the agreement between observations and modeled SI12 responses is quite good. As for the WIC signal, the shape of the SI12 signal is also characterized by first a crossing of the auroral oval, followed by the polar cap and then a second oval crossing. In Figure 7, corresponding to the case b in Table 2 and illustrated in Figure 2b, the polar cap crossing between 1410 and 1420 UT presents a weak continuous emission. This is probably the signature of the polar rain which are low-energy solar wind particles precipitating into the atmosphere along the opened magnetospheric field lines poleward of the auroral zone. *Fairfield and Scudder* [1985] demonstrated that the more energetic component of the polar rain is composed of charged particles from the solar wind "strahl," a field-aligned component of the solar wind. In this case b, the intensity and the width of the oval crossing around 0810 MLT are well reproduced by the simulated signal. However, around 1850 MLT the calculated signal does not correctly reproduce the width of the peak even though the intensity of both signals seems to be quite well matched. This discrepancy was also present in the comparisons with the FAST measurements [*Frey et al.*, 2001; *Gérard et al.*, 2001]. Figure 8 presents a second example of comparison between SI12 calculated and observed signal, illustrated by Figure 2f and whose characteristics are summarized in Table 2-case f. In Figure 8, the agreement around the secondary peaks (between 0151 and 0157 UT) is not good. However, the maximum observed count rates are only about 3 while the simulated one reaches 1 count. Those count rates are very small and cannot be considered as significant as may be seen from the size of the error bars. The standart deviation on the count rate of these observations is about 1 count.

[31] The integration of both the actual and simulated SI12 counts over the oval a number of crossings is displayed in

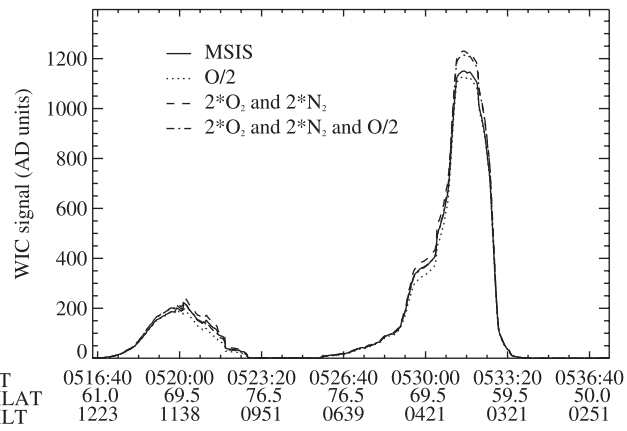

Figure 6. Sensitivity test of the influence of the atmospheric composition for case i – 7 December 2000. The solid line is the model integrated result using the MSIS-90 atmosphere. Halving the O density produces no noticable effect (dotted line). Doubling the N_2 and the O_2 density (dashed line) increases the LBH emission. The addition of both previous perturbations (dashed-dotted line) leads to an increase of the observed signal.

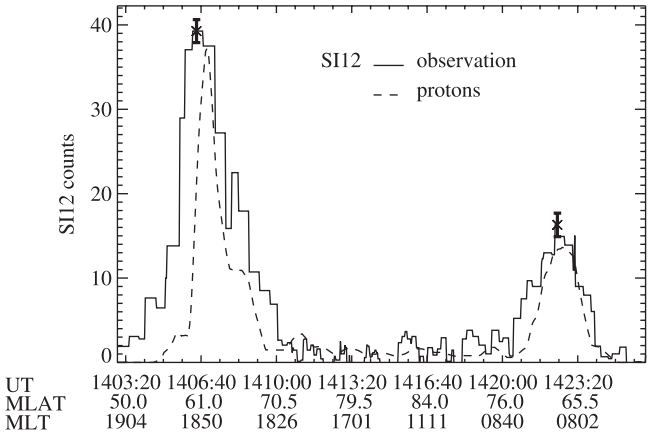

Figure 7. Comparison of the observed SI12 (solid line) and the expected SI12 signals from simulations using NOAA in situ measurements (dashed line) for case b – 15 July 2000. The error bars represent ± one standard deviation on typical observations.

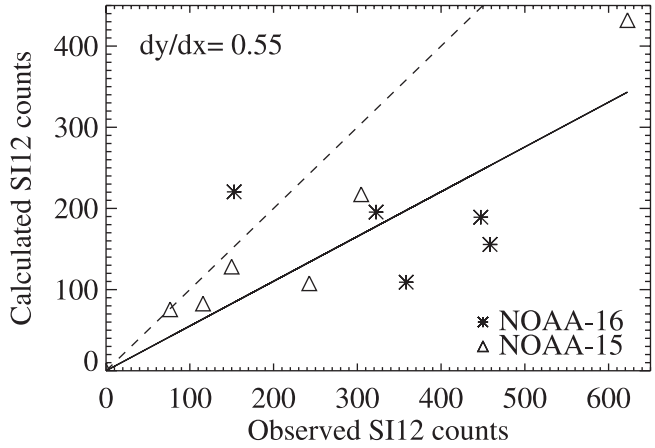

Figure 9. Observed and simulated SI12 counts summed over oval crossings. A least squaress regression (solid line) gives a slope of 0.55 ± 0.04. The dashed line corresponds to a perfect agreement between observations and simulations. The size of the horizontal error bars is similar to the size of the symbol.

Figure 9 which shows all the individual data points. All the cases illustrated in Figure 2 were used for this analysis, except case b which was removed from the analysis because it was apparently aberrant. The slope of the regression line is 0.55 ± 0.04. This result is consistent with the disagreements between the width of observed and simulated auroral oval as illustrated in Figure 7. The agreement is not as good as for WIC (see Figure 5), but we consider it is still quite acceptable in view of all the uncertainties as discussed in section 4.

[32] In this case varying the ratio O/N_2 from the MSIS model does not significantly influence the calculated emission rate because the Ly α emission is directly produced by precipitating protons. The calculated Ly α efficiencies are expected to remain virtually unchanged when altering the density of O and N_2 in comparison with MSIS. Simulations with the Monte Carlo model show that the SI12 count rate responds only very moderately to composition changes. For example, for proton with a kappa distribution with $E_0 = 1$ keV, an incident flux of 1 mW/m^2 gives an estimated Ly α brightness of 5.94 kR with the MSIS-atmosphere for a vertical view, implying about 36 SI12 counts per pixels. In dividing the neutral oxygen density by a factor of 2, which is an extreme case, the evaluated SI12 count rate becomes 33.2. The reduction of O density by a factor of 2 and the doubling of the N_2 density result in a count rate of 32.6.

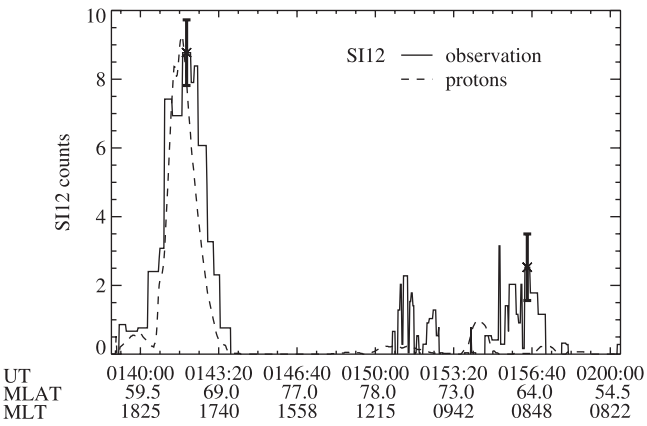

Figure 8. Same as Figure 7 for case f – 12 August 2000.

4. Contribution of High-Energy Particles

[33] Some previous similar studies [*Liou et al.*, 1999] did not take high-energy particles in consideration because most low altitude satellites have only particle detectors sensitive to less than 30 keV particles. The MEPED experiment provides the possibility to analyze the importance of protons of energy higher than 30 keV in the FUV auroral brightness. Figure 10 shows the contributions of protons with energies less and higher than 30 keV in the total energy flux for a

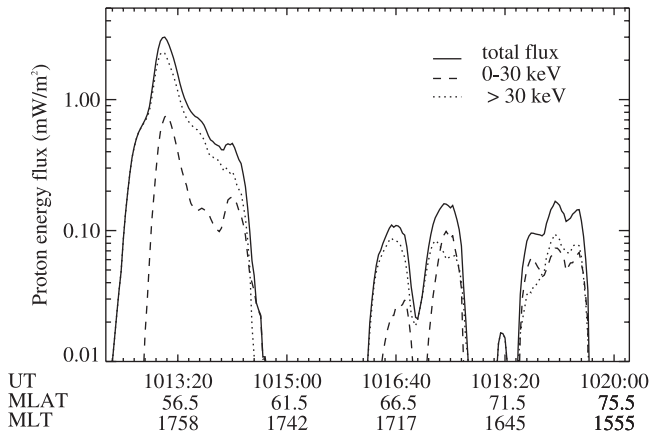

Figure 10. Variation of the proton energy flux measured along the NOAA-TIROS orbit during the first auroral oval crossing on case c – 12 August 2000. The solid line shows the total energy flux. The dashed line represents the contribution of low-energy protons from the TED measurements using an extrapolation up to 30 keV. The dotted line shows the MEPED measurements.

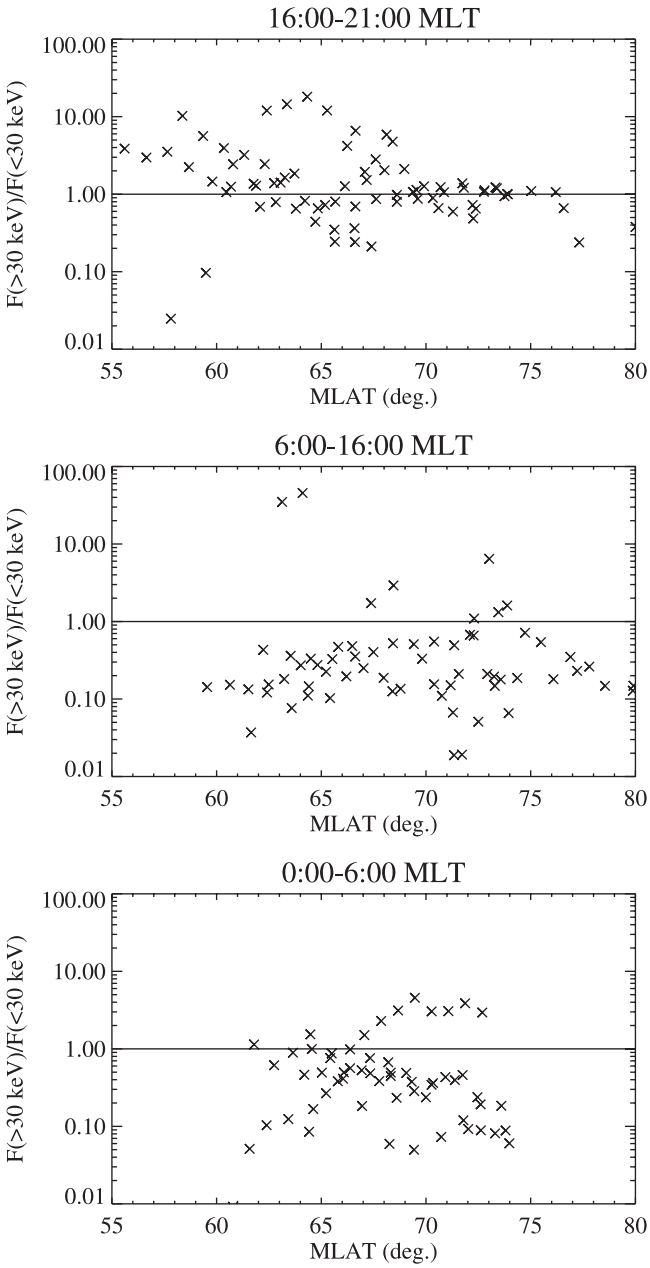

Figure 11. Ratio of the high-energy to the low-energy proton energy flux for all cases listed in Table 2 as a function of the latitude for three different magnetic local time sectors. The solid line indicates where the contributions of high-energy and low-energy protons are equal.

NOAA-15 transit of the polar region on 12 August 2000 (case c in Table 2). In this example, the high-energy proton contribution locally dominates the low-energy one: the mean contribution of low-energy protons along this oval crossing is 24%. The contribution of high-energy protons in the total energy flux as a function of the MLT sector may be statistically analyzed. In order to perform this analysis we calculate the ratio between energy fluxes carried by high (>30 keV) and low (<30 keV) energy protons averaged over 20 s of NOAA data. In so doing, we neglect the in situ measurements where the proton incident energy flux was lower then 0.05 mW/m^2. Figure 11 displays the calculated ratios for all cases illustrated in Figure 2 as a function of the magnetic latitude in three local time sectors. The results in Figure 11 encompass all levels of magnetic activity. A ratio higher than 1.0 means that the contribution of high-energy protons to the total flux is over 50%. The three different local time sectors were determined from the magnetic footprint crossed by the NOAA satellites. One region extends on the dusk sector between 1600 and 2100 MLT, another sector includes the postmidnight aurora and the last one covers the dayside sector between 0600 and 1600 MLT. In the dusk sector, high-energy protons significantly dominate the precipitating proton flux near the equatorward boundary

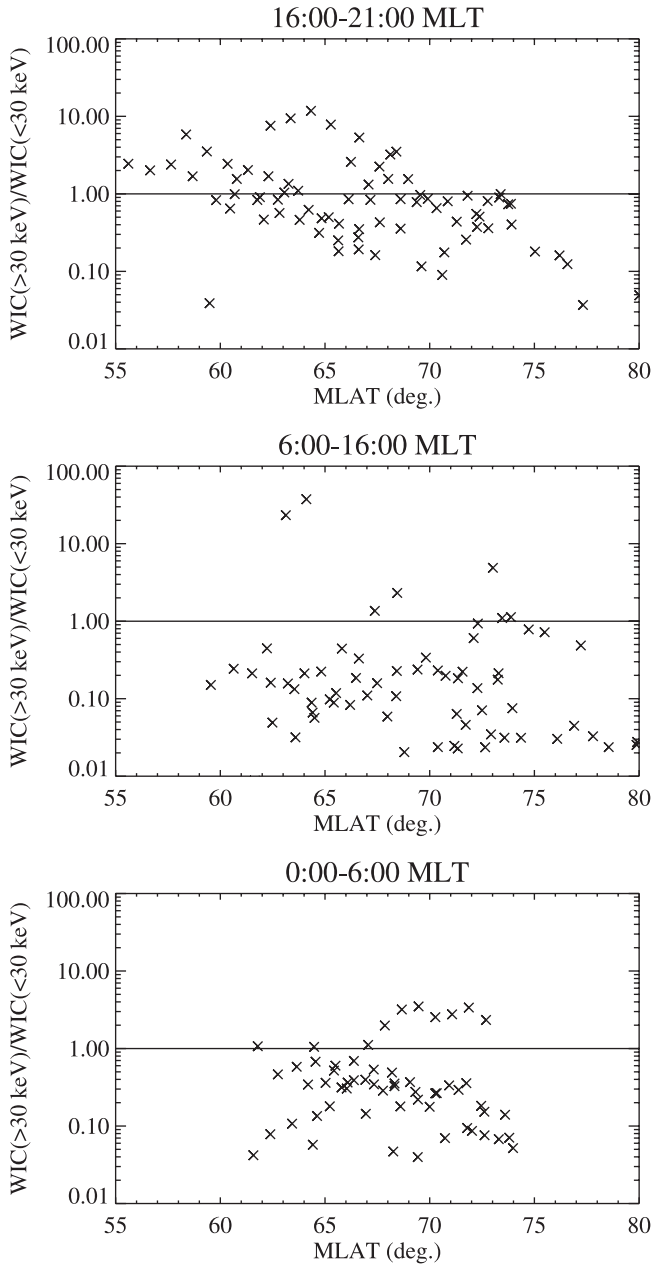

Figure 12. Ratio of high-energy and low-energy proton contribution to the WIC signal for all cases listed in Table 2. The solid line indicates where the contributions of high-energy and low-energy protons are equal.

of the auroral oval. Below 65°N the mean contribution in energy flux of high-energy protons is 8.2 times larger than the contribution of low-energy protons. Near the polar boundary the mean ratio is 0.93 so the mean energy flux due to high-energy protons is around 50% of the total energy flux. In the sector between 0600 and 1600 MLT, the major portion of energy flux is carried by low-energy protons, as indicated by the mean ratio of 0.43. In the postmidnight sector, the relative contribution of the high-energy component is higher than 50% only for the NOAA-16 crossing around 0609 UT on 23 December 2000. This is probably an isolated injection event as the Kp index over the previous 3-hours was 6. These results are in agreement with the statistical model of ion precipitation by *Hardy et al.* [1989] based on DMSP data. The particle detectors on board the DMSP satellites covered the energy range 30 eV to 30 keV. When the derived mean energy is close to 30 keV, it is likely that the real mean energy exceeds this limit as the Maxwellian extrapolation probably underestimated the actual value. The study from *Hardy et al.* [1989] also shows that in the dusk sector the proton mean energy increases for decreasing latitudes. Moreover, the average proton energy is the lowest in the dayside sector between 0600 and 1200 MLT.

[34] We analyzed the contribution of protons of energy greater than 30 keV and less than 30 keV to the simulated WIC signal by calculating the relative contributions of high and low-energy proton to the modeled WIC counts (Figure 12). They are quite similar to those of Figure 11 obtained for the energy flux, but a smaller fraction of the WIC ratios are above the limit of 1.0. This means that the relative contribution of high-energy protons in the WIC signal is less important than in the energy flux. WIC efficiencies due to incident protons vary with proton mean energy but no substantial variation occurs near or above 30 keV. However, the amount of O_2 absorption increases for increasing energy so that high-energy protons produce emission that is more efficiently absorbed by O_2. For electrons, the proportion above 30 keV is insignificant to the WIC signal. Even under very intense events when the contribution of high-energy electrons to the total energy flux can reach 30%, the resulting LBH emission is negligible. This is because high-energy electrons reach lower altitudes so that the emission they produce is strongly absorbed by O_2.

5. Discussion and Conclusions

[35] The results of the comparison described in the preceding sections (Figures 5 and 9) show statistical agreements between observations and model calculations of about 70% for the WIC signal and about 55% for the SI12 signal, both of which we consider as very satisfactory. For WIC—in situ comparisons several different explanations for the remaining discrepancy can be suggested. First, there are uncertainties associated with the calibration of the MEPED and TED instruments. On the basis of preflight calibrations and comparisons between NOAA-15 and NOAA-16 observations at nearly the same locations and times, the uncertainty in the TED energy flux measurements is estimated to about ±25% for energy fluxes of above 1 mW/m^2 while the error in the mean energy can be approximately one channel. Second, a part of the disagreement can be assigned to the assumptions about the precipitating particles. The TED instrument measures particles less than 20 keV at two pitch angles, both within the loss cone. In contrast, we used only the MEPED measurements at the pitch angle within the loss cone and calculated the total flux incident on the atmosphere assuming isotropy over the loss cone. If the incident energetic particles were not isotropic, this assumption could lead to an underestimate of the actual incident fluxes. When proton fluxes are significant, their angular distribution is generally isotropic and so probably cannot fully explain the disagreements. Radiation damage to the MEPED proton solid state detectors is another potential source of error especially for data from the NOAA-15 satellite that had been in operation for over two years. The effect of radiation damage is to increase the proton energy thresholds over their original values and, if not taken into account, leads to an underestimate of the >30 keV energy flux to the atmosphere. Because comparisons with NOAA-16 observations also lead to underestimates of the SI12 signal (Figure 9), radiation damage is unlikely to fully account for the discrepancies.

[36] The models we use can also introduce some error. As described in section 3.1, the MSIS model that calculates the atmospheric composition profile can introduce errors in the WIC-in situ comparisons. It is probable that local density variations are not reproduced by the model and so the calculation may underestimate the real emission brightness. In addition, errors can stem from the cross sections used in models [*Kanik et al.*, 2000]. For example, previous studies [*Eastes and Dentamaro*, 1996; *Eastes*, 2000] indicate that *Ajello and Shemansky*'s [1985] LBH cross section used in the GLOW model for electrons may be underestimated owing to the presence of three close-lying states (a $^1\Pi_g$, a′ $^1\Sigma_u^-$ and w $^1\Delta_u$) of N_2. The a′ $^1\Sigma_u^-$ and w $^1\Delta_u$ states are long-lived and optically forbidden to the ground state but are optically allowed to the a $^1\Pi_g$ state. Cascading from these two states can induce in the upper atmosphere a 30% additional contribution to the direct LBH cross section. In the case of SI12, the uncertainties in instrument calibration, in cross section values used in models all contribute to the disagreement. Moreover, space and time averaging, dayglow subtraction, IMAGE detector calibration and limited resolution are also potential sources of uncertainties.

[37] Considering all sources of errors, we conclude that the observed FUV intensities are in accordance with intensities predicted from in situ NOAA measurements. The FUV observations from the WIC and SI12 instruments can thus be used for quantitative analyses and determination of auroral particle precipitation. We have shown that auroral particle energy flux information may be extracted from global observations of the auroral region separately for protons and for electrons. The WIC and SI12 instruments are shown capable of observing the temporal evolution of auroral particle injection to the ionosphere on a spatially global basis.

[38] Characterization of proton precipitation using NOAA in situ measurements and FUV observations gives results in agreement with the *Hardy et al.* [1989] precipitation model. The results confirm that in the dusk sector the proton auroral oval is shifted equatorward of the electron one and high-energy protons contribution is more important at low latitudes. In the other local time sectors the high-energy

proton contribution does not play such an important role. We have shown that auroral protons locally contribute substantially to ionosphere characteristics, in particular ionization and heating at high latitudes.

[39] **Acknowledgments.** V. Coumans is supported by a fellowship from the Belgian Fund for Research in Industry and Agriculture (FRIA) and J.-C. Gerard by the Belgian National Fund for Scientific Research (FNRS). This work was funded by the PRODEX program of the European Space Agency (ESA). We acknowledge S. B. Mende of the University of California, Berkeley, who is the Principal Investigator on the IMAGE-FUV. We thank V. I. Shematovich and D. V. Bisikalo for their help in the determination of proton emission efficiencies and their assistance in using the models. We thank the referees for their useful suggestions.

[40] Arthur Richmond thanks Frederick Rees and another reviewer for their assistance in evaluating this paper.

References

Ajello, J. M., and D. E. Shemansky, A reexamination of important N_2 cross sections by electron impact with application to the dayglow: The Lyman-Birge-Hopfield band system and N I (119.99 nm), *J. Geophys. Res.*, *90*, 9845, 1985.

D. Bilitza, (Ed.), *International Reference Ionosphere 1990, NSSDC 90-22*, Natl. Space Sci. Data Cent., Greenbelt, Md, 1990.

Burch, J. L., Image mission overview, *Space Sci. Rev.*, *91*, 1, 2000.

Eastes, R. W., Modeling the N_2 Lyman-Birge-Hopfield bands in the dayglow: Including radiative and collisional cascading between the singlet states, *J. Geophys. Res.*, *105*, 18,557, 2000.

Eastes, R. W., and A. V. Dentamaro, Collision-induced transitions between the $a^1\Pi_g$, $a'\ ^1\Sigma_u^-$, and $w^1\Delta_u$ states of N_2: Can they affect auroral N_2 Lyman-Birge-Hopfield band emissions?, *J. Geophys. Res.*, *101*, 26,931, 1996.

Fairfield, D. H., and J. D. Scudder, Polar rain: Solar coronal electrons in the Earth's magnetosphere, *J. Geophys. Res.*, *90*, 4055, 1985.

Frey, H. U., S. B. Mende, C. W. Carlson, J.-C. Gérard, B. Hubert, J. Spann, R. Gladstone, and T. J. Immel, The electron and proton aurora as seen by IMAGE-FUV and FAST, *Geophys. Res. Lett.*, *28*, 1135, 2001.

Fuller-Rowell, T. J., and D. S. Evans, Height-integrated Pedersen and Hall conductivity patterns inferred from the TIROS-NOAA satellite data, *J. Geophys. Res.*, *92*, 7606, 1987.

Gérard, J.-C., B. Hubert, D. V. Bisikalo, and V. I. Shematovich, A model of Lyman-α line profile in the proton aurora, *J. Geophys. Res.*, *105*, 795, 2000.

Gérard, J.-C., B. Hubert, M. Meurant, V. Bisikalo, I. Shematovich, H. U. Frey, S. B. Mende, G. R. Gladstone, and C. W. Carlson, Observation of the proton aurora with IMAGE FUV imager and simultaneous ion flux in-situ measurements, *J. Geophys. Res.*, *106*, 28,939, 2001.

Hardy, D. A., M. S. Gussenhoven, and D. Brautigam, A statistical model of auroral ion precipitation, *J. Geophys. Res.*, *94*, 370, 1989.

Hecht, J. H., D. L. McKenzie, A. B. Christensen, D. J. Strickland, J. P. Thayer, and J. Watermann, Simultaneous observations of lower thermospheric composition change during moderate auroral activity from Kangerlussuaq and Narsarsuaq, Greenland, *J. Geophys. Res.*, *105*, 27,109, 2000.

Hedin, A. E., Extension of the MSIS thermosphere model into the middle and lower atmosphere, *J. Geophys. Res.*, *96*, 1159, 1991.

Hubert, B., J.-C. Gérard, D. V. Bisikalo, V. I. Shematovich, and S. C. Solomon, The role of proton precipitation in the excitation of the auroral FUV emissions, *J. Geophys. Res.*, *106*, 21,475, 2001.

Kanik, I., L. W. Beegle, J. M. Ajello, and S. C. Solomon, Electron-impact excitation/emission and photoabsorption cross sections important in the terrestrial airglow and auroral analysis of rocket and satellite observations, *Phys. Chem. Earth, Part C*, *25*, 573, 2000.

Liou, K., P. T. Newell, C.-I. Meng, T. Sotirelis, M. Brittnacher, and G. Parks, Source region of 1500 MLT auroral bright spots: Simultaneous Polar UV-images and DMSP particle data, *J. Geophys. Res.*, *104*, 24,587, 1999.

Marov, M. Y., V. I. Shematovich, D. V. Bisikalo, and J.-C. Gérard, *Nonequilibrium Processes in Planetary and Cometary Atmosphere: Theory and Applications*, Kluwer Acad., Norwell, Mass., 1997.

Mende, S. B., et al., Far ultraviolet imaging from the IMAGE spacecraft, 1, System design, *Space Sci. Rev.*, *91*, 243, 2000.

Mende, S. B., H. U. Frey, M. Lampton, J.-C. Gérard, B. Hubert, S. Fuselier, J. Spann, R. Gladstone, and J. L. Burch, Global observations of proton and electron auroras in a substorm, *Geophys. Res. Lett.*, *28*, 1139, 2001.

Østgaard, N., J. Stadsnes, J. Bjordal, R. R. Vondrak, S. A. Cummer, D. L. Chenette, G. K. Parks, M. J. Brittnacher, and D. L. McKenzie, Global-scale electron precipitation features seen in UV and X rays during substorms, *J. Geophys. Res.*, *104*, 10,191, 1999.

Østgaard, N., J. Stadsnes, J. Bjordal, R. R. Vondrak, S. A. Cummer, D. L. Chenette, M. Schultz, and J. G. Pronko, Cause of the localized maximum of X-ray emission in the morning sector: A comparison with electron measurements, *J. Geophys. Res.*, *105*, 20,869, 2000.

Robinson, R. M., R. R. Vondrak, J. D. Craven, L. A. Frank, and K. Miller, A comparison of ionospheric conductances and auroral luminosities observed simultaneously with the Chatanika radar and the DE 1 auroral imagers, *J. Geophys. Res.*, *94*, 5382, 1989.

Senior, C., J. R. Sharber, J. D. Winningham, O. de la Beaujardière, R. A. Heelis, D. S. Evans, M. Sugiura, and W. R. Hoegy, *E* and *F* region study of the evening sector auroral oval: A Chatanika/Dynamics Explorer 2/NOAA 6 comparison, *J. Geophys. Res.*, *92*, 2477, 1987.

Solomon, S. C., P. B. Hays, and V. Abreu, The auroral 6300 Å emission: Observation and modeling, *J. Geophys. Res.*, *93*, 9867, 1988.

Strickland, D. J., R. E. Daniell Jr., J. R. Jasperse, and B. Basu, Transport-theoretic model for the electron-proton-hydrogen atom aurora, 2, Model results, *J. Geophys. Res.*, *98*, 21,533, 1993.

V. Coumans, J.-C. Gérard, and B. Hubert, Laboratoire de Physique Atmosphérique et Planétaire, Université de Liège, Belgium.

D. S. Evans, NOAA Space Environment Center, Boulder, Colorado, USA.